Fusion near and below the barrier for the systems $^{32,34}S+^{24,25,26}Mg$ and $^{32}S+^{27}Al$

G. M. Berkowitz,* P. Braun-Munzinger, J. S. Karp, R. H. Freifelder, T. R. Renner,† and H. W. Wilschut‡
Department of Physics, State University of New York, Stony Brook, New York 11794
(Received 25 April 1983)

Excitation functions are reported for total fusion near and below the Coulomb barrier of the systems $^{32,34}S+^{24,25,26}Mg$ and ^{27}Al. The data cannot be reproduced by one-dimensional barrier penetration calculations. The enhancement of the cross sections at low energies is compared to predictions of models taking into acount the static deformation or zero point vibration of the reaction partners. Calculations including zero point motion do not reproduce the observed variations of the measured cross sections with respect to the neutron number of target and projectile. Reasonable agreement is obtained when calculating fusion between statically deformed nuclei. Finally, the fusion process is described in a quantum mechanical coupled channels model, indicating the importance of dynamical effect on sub-barrier fusion.

[NUCLEAR REACTIONS $^{24,25,26}Mg$, $^{27}Al(^{32,34}S$, Fusion) $0.9<E_{c.m.}/E_{Coul}<1.1$; measured evaporation residues, deduced barrier parameters; discussed importance of zero point motion, static deformation, coupled channels effects on fusion process.]

I. INTRODUCTION

It is by now well established[1-5] that for energies well below the *s*-wave interaction barrier the cross section for total fusion between sufficiently heavy ions is significantly larger than predicted in conventional, one-dimensional barrier penetration models. The precise mechanism leading to this enhancement is not well understood. Macroscopic effects such as neck formation between reactants have been invoked[1,2,5] as well as more microscopic explanations based on static deformations,[3] the influence of valence nucleons[4,6] or fluctuations of the nuclear shapes due to zero point motion[7-9] or dynamical effects during the reaction.[10] While all these models predict sub-barrier enhancements similar to what has been observed experimentally the influence of specific nuclear structure effects has, until now, not been convincingly demonstrated. This is mostly due to the limited number of systems for which systematic studies of fusion cross sections at sub-barrier energies have been undertaken.

In order to shed more light on the role of nuclear structure in fusion reactions we have studied complete fusion excitation functions for the systems $^{32,34}S+^{24,25,26}Mg$ and $^{32}S+^{27}Al$ over a range of energies from above to well below the *s*-wave fusion barrier. Data were taken by directly identifying the evaporation residues in an ionization-chamber–solid-state-detector telescope.

Experimental details of the data acquisition and analysis are given in Sec. II. The experimental results are described in Sec. III. An analysis of the measured excitation functions is presented in Sec. IV in terms of simple, one dimensional models. There, the emphasis is on extracting phenomenological barrier parameters and on deducing possible enhancements of the measured cross sections compared to the predictions of one-dimensional models.

Section V contains a discussion of models for the fusion process incorporating vibrational zero point motion or static deformation of the colliding nuclei and comparison of their prediction with the measured data. Similarly to the approach described in Ref. 8, the additional degrees of freedom are incorporated into semiclassical calculations of barrier penetrabilities. An important ingredient of all these models is the assumption that the nuclear shapes are "frozen" during the actual fusion process. This adiabatic assumption is discussed by estimating the time scale of the fusion process from the "time delay" encountered by the ions during the barrier penetration process.

Within these models there are, in principle, no new free parameters since the nuclear structure of the sulfur and magnesium isotopes is rather well known. Comparison of the predictions of these models with the present data should then elucidate the role played by this structure in the fusion process.

In semiclassical models it is, however, rather difficult to take into account dynamical effects such as real (or virtual) excitation of low lying states of the nuclei on their way to fusion. In order to further investigate this aspect, a brief discussion is presented in Sec. VI, of the results of quantum mechanical coupled channels calculations for the elastic scattering and excitation of relevant low lying states at energies near the interaction barrier. In this approach, the fusion cross section is obtained as the difference between the total reaction cross section and the quasielastic cross section. In such a quantum mechanical calculation, effects such as zero point motion and/or dynamic and static deformations are, in principle, correctly taken into account, albeit at the expense of having to introduce a (rather poorly known) absorptive part into the nucleus-nucleus interaction. Comparison of the predictions of this model with the detailed isotopic dependence of the measured fusion cross section may provide information on the relevance of such a description and the importance of dynamical effects during the fusion process.

II. EXPERIMENTAL METHOD

The experiments used the ^{32}S and ^{34}S beams from the Stony Brook FN Tandem Van de Graaff accelerator to bombard targets of isotopically enriched ($\gtrsim 98\%$) $^{24,25,26}Mg$ and ^{27}Al. The Mg targets were evaporated onto a thin ($\sim 10\ \mu g/cm^2$) carbon backing; the Al targets were self-supporting. The thickness of the targets ranged between 50 and 200 $\mu g/cm^2$ areal density as measured via the energy loss of α particles from a ^{241}Am source.

Elastically scattered particles and evaporation residues following fusion reactions were identified in an ionization counter Si surface barrier detector telescope. The telescope had an entrance window of stretched polypropylene ($\sim 75\ \mu g/cm^2$ areal density) and was operated at gas pressures of less than 10 Torr of Ar (90%)-CH_4 (10%) to minimize losses of low energy heavy mass evaporation residues. The telescope subtended a solid angle of 8×10^{-5} sr with an angular opening of $\pm 0.3°$, allowing measurements at angles as small as $\theta_{lab}\approx 2.5°$. Two symmetrically placed monitor detectors served to check the position of the beam and were used for normalization of the angular distribution measurements. The ΔE and energy resolution of the telescope was sufficient to cleanly separate evaporation residues from elastically scattered particles and fusion products from the carbon and oxygen contaminants in the target even at the lowest bombarding energies. This is evident from Fig. 1, where a ΔE-E density plot for the system $^{32}S+^{25}Mg$ is shown, obtained at $\theta_{lab}=8°$ and $E_{lab}=62$ MeV.

To obtain excitation functions for total fusion, single angle excitation functions were measured for the systems $^{32}S+^{27}Al$ and $^{32,34}S+^{24,25,26}Mg$. Evaporation residues were detected at incident energies ranging from $E_{lab}=60$ to 75 MeV in steps of $\Delta E_{lab}=1$ MeV. Data were taken at $\theta_{lab}=8°$ for all systems except $^{32}S+^{24}Mg$ where the scattering angle was 10°. In order to normalize the single angle excitation functions, complete evaporation residue angular distributions were measured in the angular range $3\leq\theta_{lab}\leq 16°$ at energies of $E_{lab}=68$ and 75 MeV for all systems except $^{32}S+^{27}Al$ where data were obtained only at 75 MeV.

The relative cross section scale of the single angle excitation functions and angular distributions was established by normalizing the evaporation residue yields to the yields for elastic scattering which at the previously mentioned angles and energies follow the Rutherford law. The angular distribution measurements at larger angles ($\theta_{lab}\geq 14°$) allowed the separation of the elastic peaks due to S + Mg scattering from the peaks corresponding to scattering off carbon and oxygen contaminants in the targets. Since the latter cross sections also follow Rutherford scattering, the amount of contamination could be determined directly. Measurements at other angles and energies were correspondingly corrected for the presence of these contaminants, thereby establishing the absolute cross section scales.

Repeat points in the angular distribution measurements ensured that the relative error in these data was less than 5%. The absolute errors in the single angle excitation functions are estimated to be smaller than 10% and up to 20% at the lowest energies where poor statistics furnished the major contribution to the error bars.

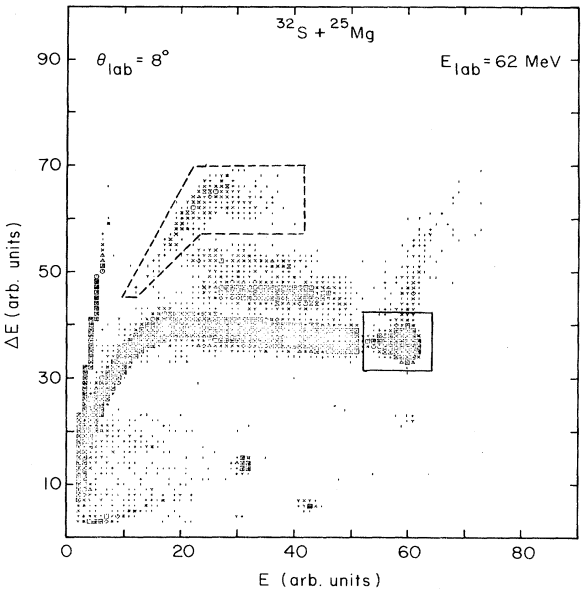

FIG. 1. ΔE-E density plot for $^{32}S+^{25}Mg$ at $\theta_{lab}=8°$ and $E_{lab}=62$ MeV, uncorrected for energy loss in the target. The elastic peaks are in the region of high E and low ΔE enclosed by the solid line. The fusion events are in the region of high ΔE and intermediate E enclosed by the dashed line.

III. EXPERIMENTAL RESULTS

Single angle excitation functions for total fusion are presented in Figs. 2 and 3 for the systems $^{32}S+^{27}Al$ and $^{32,34}S+^{24,25,26}Mg$ as a function of center of mass energy. For all systems, the energy scale has been corrected for the energy loss in the target. All excitation functions are structureless and exhibit a strong decrease at energies below $E_{c.m.}\approx 8$ MeV which roughly corresponds to the s-wave barrier for the present systems (see below).

Angular distributions measured at $E_{lab}=68$ and 75 MeV are displayed in Figs. 4 and 5 in the form of $d\sigma/d\theta$ versus laboratory scattering angle. They are compared to results of statistical model calculations using the Monte Carlo code Julian/Pace.[11] The shapes of the measured angular distributions agree rather well with the statistical model predictions although for some systems ($^{32}S+^{24,25}Mg$) the predicted cross section exceeds the experimental values at angles near $\theta_{lab}=10°$. The absolute normalization of the calculated angular distributions depends on the cross section for total fusion which was adjusted to reproduce the measured data.

For all systems the total fusion cross section was obtained by integrating the measured angular distributions. For this purpose cross section values corresponding to scattering angles $\theta_{lab}>16°$ can safely be neglected as is obvious from inspection of Figs. 4 and 5. More problematic is the extrapolation of the data towards zero degrees; the experimental setup did not allow measurements at angles $\theta_{lab}\leq 2.5°$ which yielded a small measure of uncertainty in this extrapolation (see Figs. 4 and 5). Two independent procedures were, therefore, adopted for the evaluation of

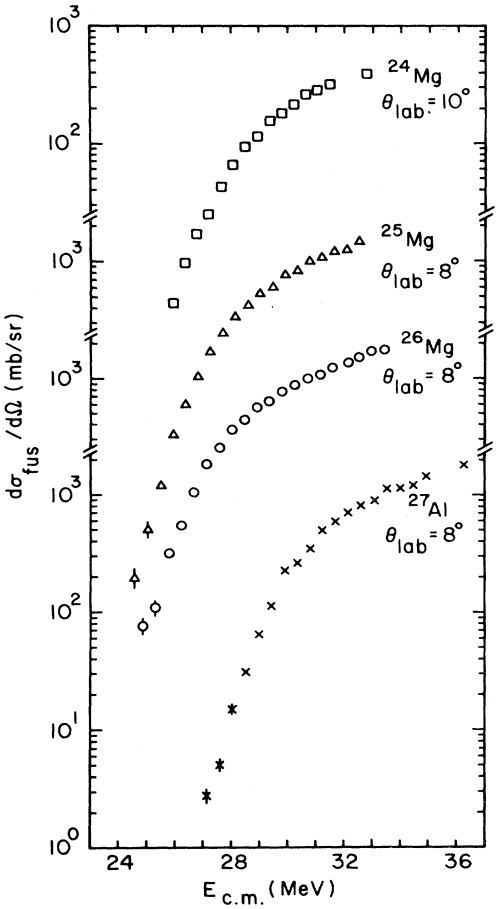

FIG. 2. Single angle excitation functions for total fusion as a function of c.m. energy for ^{32}S induced reactions.

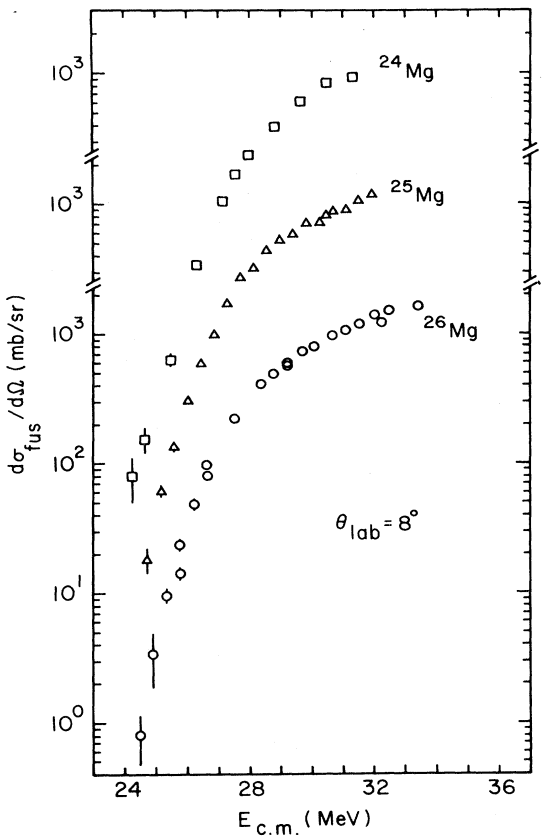

FIG. 3. Single angle excitation functions for total fusion as a function of c.m. energy for ^{34}S induced reactions.

the cross section integral. First, the differential cross section $d\sigma/d\Omega$ was fitted in the angular range $2.5<\theta_{lab}<8°$ by a zero centered Gaussian. The integral of the angular distribution was then obtained by integrating the Gaussian starting at zero degrees up to the smallest angle for which cross sections were measured and completing the integration using the measured data. As a second estimate similar integrations were performed by using the results of the statistical model calculations for the angular distributions, at $\theta_{lab}=0.5°$, 1.5°, and 2.5°, in the numerical integration procedure. The results from these two procedures agreed to within 4% for all systems, indicating the size of systematic errors in the data. In the following, all total fusion cross sections are based on the second procedure, i.e., extrapolation of the measured cross sections using the results of the statistical model calculations. In particular, the integrals of the angular distributions at $E_{lab}=68$ and 75 MeV were used to convert the single angle excitation functions into excitation functions for total fusion. This assumes that the shape of the evaporation residue angular distributions does not appreciably change within the energy range considered. This is supported by the statistical model calculations and by the fact that the energy dependence of the integrated angular distributions is in good agreement with the results from the single angle excitation functions.

Excitation functions for total fusion are displayed in Figs. 6 and 7 for all systems studied in the present investigation. In the following chapters, these experimental results will be compared to the predictions of various different models in order to establish the degree of subbarrier enhancement and to elucidate the underlying reaction mechanism.

IV. COMPARISON OF THE DATA WITH THE PREDICTIONS OF ONE-DIMENSIONAL MODELS

In a simple, phenomenological approach, fusion between two nuclei is assumed to take place if the reaction partners pass through or over their interaction barrier. The cross section for complete fusion can then be simply decomposed into contributions from different partial waves according to

$$\sigma_{fus}=\pi\lambda\!\!\!^{-2}\sum_{l=0}^{\infty}(2l+1)T_l\ , \tag{1}$$

where $\lambda\!\!\!^{-}$ is the reduced wavelength of relative motion and the penetration coefficient T_l describes the barrier penetra-

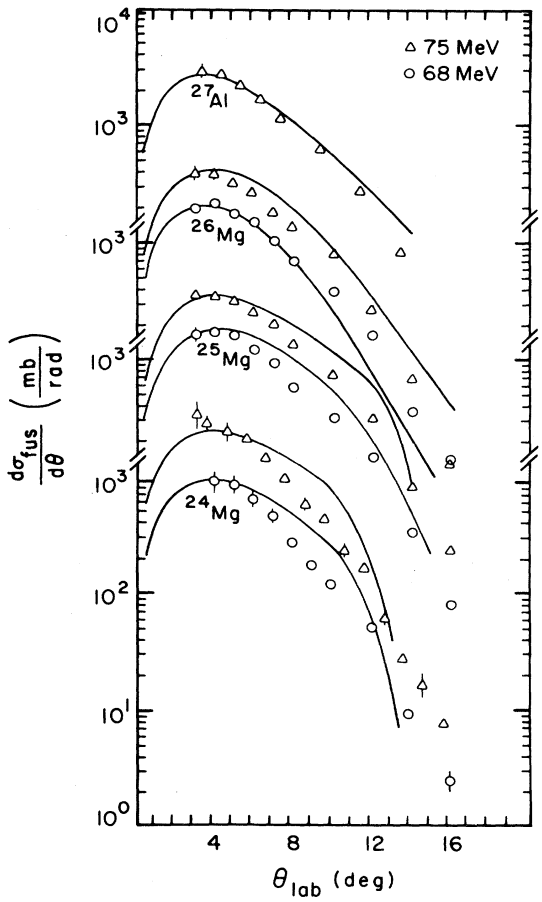

FIG. 4. Angular distributions for ^{32}S induced reactions at $E_{lab}=68$ (circles) and 75 (triangles) MeV. Solid curves are statistical model calculations as explained in the text.

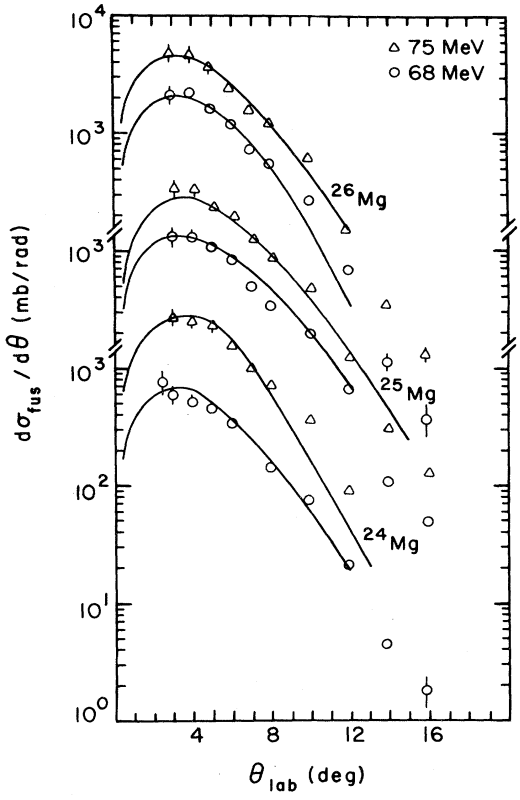

FIG. 5. Angular distributions for ^{34}S induced reactions at $E_{lab}=68$ (circles) and 75 (triangles) MeV. Solid curves are statistical model calculations as explained in the text.

tion. Implicit in Eq. (1) is the neglect of any frictional forces or dissipation and spin orbit forces in the ion-ion interaction. For central one-dimensional potentials, the penetration coefficients T_l can be obtained by integrating the Schrödinger equation or, alternatively, by making use of the WKB approximations, i.e.,

$$T_l=\frac{1}{1+\exp(S_l)}\ , \tag{2a}$$

where the classical action S_l is evaluated between the outer and inner turning points r_1 and r_2 according to

$$S_l=2\int_{r_1}^{r_2}\left[\frac{2\mu}{\hbar^2}(V_l-E_{c.m.})\right]^{1/2}dr\ . \tag{2b}$$

In Eq. (2b) μ is the reduced mass, V_l the effective potential, and $E_{c.m.}$ the center of mass energy. In a first attempt to understand the measured sub-barrier fusion cross sections we have used simple, empirical nucleus-nucleus potentials[9,12] to calculate fusion cross sections according to Eqs. (1) and (2). Within the spirit of this empirical approach, the depth of the real part of the nuclear potential was allowed to vary slightly in order to ensure a good description of the data at energies above the barrier. The results of these calculations are compared to the data in Figs. 8 and 9 (solid lines). In order to correct for the variation of the s-wave barrier, the energy axis has been appropriately shifted for the various systems. At energies above the barrier, all measured fusion cross sections are well reproduced by the calculations. At lower energies ($E_{c.m.}-V_B<-1$ MeV) the calculated results are substantially smaller than the experimental data for the case of ^{32}S induced reactions, and less so but still visible for systems involving ^{34}S. This will be discussed further below. The potential parameters obtained from this simple fit procedure are collected in Table I and compared to the original parameters of Ref. 12. The enhancement of the data over the calculations at low energies is significant, especially if one takes into account the fact that the potential of Ref. 12 has a very small barrier width compared to other potentials in the literature. Taking, e.g., the potential of Ref. 13 as the starting point for such one dimensional calculations, sub-barrier enhancements of one to two orders of magnitude are obtained for all systems studied in this work.

In order to determine more quantitatively the degree of sub-barrier enhancement we have also treated the barrier width as a free parameter. This can be done conveniently

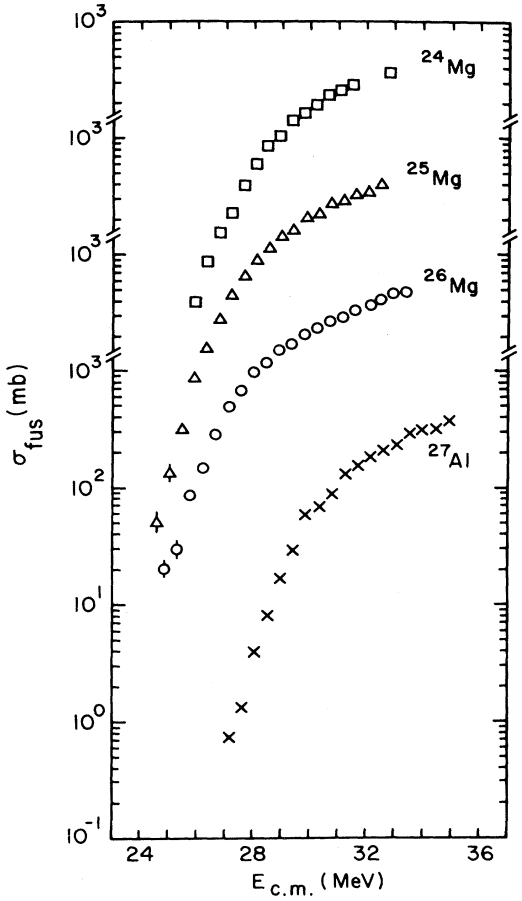

FIG. 6. Angle integrated total fusion cross sections as a function of c.m. energy for ^{32}S induced reactions.

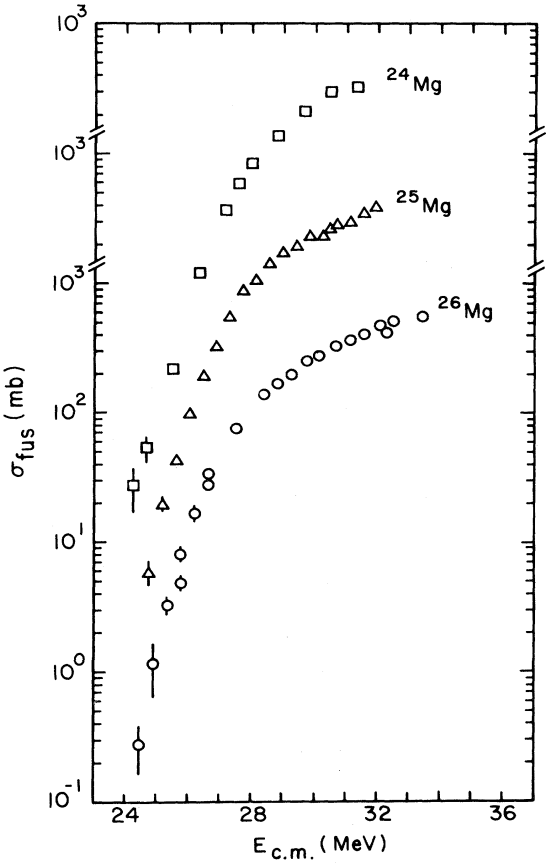

FIG. 7. Angle integrated total fusion cross sections as a function of c.m. energy for ^{34}S induced reactions.

by approximating the shape of the barrier with an inverted parabola. In this case, the sum in Eq. (1) can be performed analytically, yielding Wong's formula,[14]

$$\sigma_{\text{fus}}=\frac{R_B^2\hbar\omega}{2E_{\text{c.m.}}}\ln\left[1+\exp\left[\frac{2\pi(E_{\text{c.m.}}-V_B)}{\hbar\omega}\right]\right], \qquad (3)$$

where the fusion cross section is expressed in terms of three parameters: the s-wave barrier V_B, its position R_B, and its curvature $\hbar\omega$.[14] Using the previously determined V_B and R_B values and varying the barrier curvature $\hbar\omega$ then leads to a good description of all measured data (see dashed lines in Figs. 8 and 9). The deduced curvature values are compared in Table I to the values obtained from the original potential of Ref. 12 and indicate that a substantial reduction in barrier width is necessary in order to reproduce the observed large cross sections at subbarrier energies. In addition, one should keep in mind that, at energies well below the barrier, the parabolic approximation (which is quite unrealistic because of the Coulomb interaction) leads to substantially too large calculated cross sections.

The above results clearly indicate that the present data cannot be described by one-dimensional models unless one is willing to arbitrarily reduce the thickness of empirically determined fusion barriers to quite small values. In the following sections, we investigate such possible causes for the observed sub-barrier enhancements as zero point motion, static deformations, and effects due to the strong inelastic (Coulomb) excitation of the fragments on their way to fusion.

V. MODELS INVOLVING MORE THAN ONE DEGREE OF FREEDOM

The penetrability coefficients T_l depend sensitively on the shape of the interaction barrier as is obvious from Eq. (2). Additional degrees of freedom taken into account when calculating the interaction barrier will, therefore, directly influence the penetrabilities and, consequently, the fusion probability [see Eq. (1)]. As in Refs. 8 and 10, the effects of deviations from spherical symmetry were taken into account for the two approaching nuclei in addition to the dependence of the interaction potential on the radial separation. The influence of these additional degrees of freedom on the barrier penetration can within this approximation be calculated by "averaging" the multidimension-

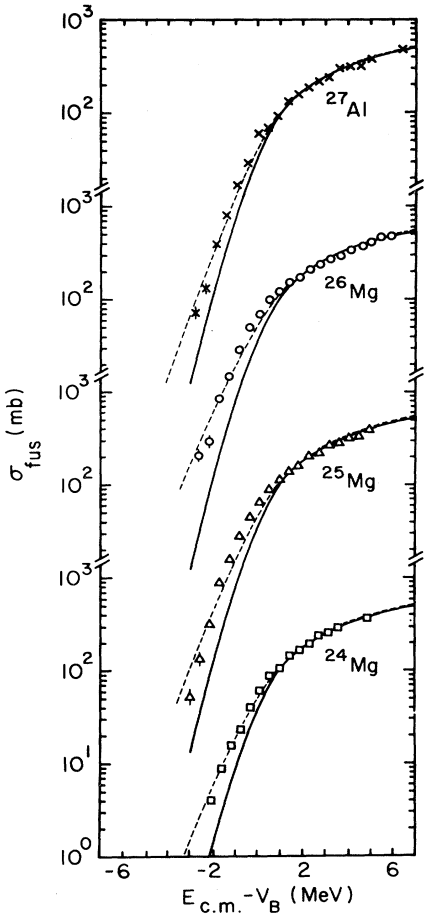

FIG. 8. Comparison of the measured excitation functions for ^{32}S induced reactions with calculated excitation functions based on a one dimensional model using the Christensen-Winther potential (Ref. 12) (solid curve) and Wong's formula (Ref. 14) (dashed curve). The energy axis of each system has been shifted by the *s*-wave potential barrier.

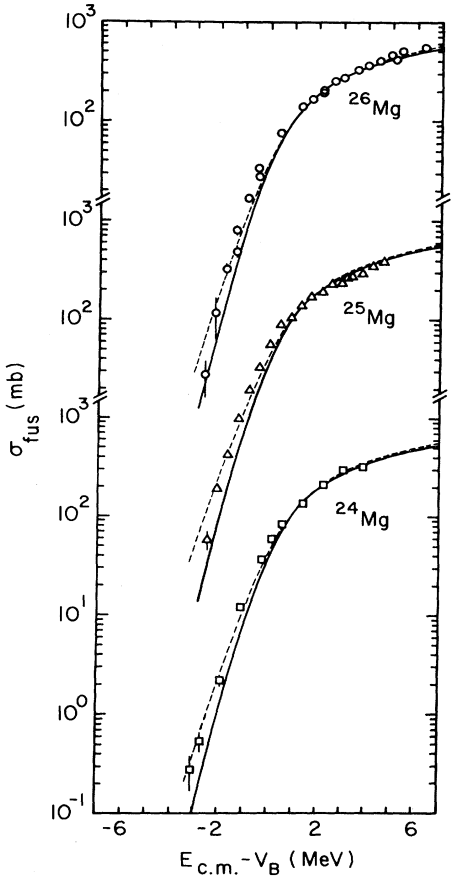

FIG. 9. Comparison of the measured excitation functions for ^{34}S induced reactions with calculated excitation functions based on a one dimensional model using the Christensen-Winther potential (Ref. 12) (solid curve) and Wong's formula (Ref. 14) (dashed curve). The energy axis of each system has been shifted by the *s*-wave potential barrier.

TABLE I. Barrier parameters for the systems investigated in the present work. The height V_B and position R_B of the interaction barrier of the potential of Ref. 12 are compared to the corresponding values V_{B_f} and R_{B_f} obtained by fitting excitation function data in the range $100 < \sigma_{fus} < 500$ mb. The curvatures $\hbar\omega_f$ for these potentials and the corresponding results $\hbar\omega$ determined from fits using Wong's formula (Ref. 14) are shown in the last columns.

System	R_B (fm)	V_B (MeV)	R_{B_f} (fm)	V_{B_f} (MeV)	$\hbar\omega_f$ (MeV)	$\hbar\omega$ (MeV)
^{32}S+^{24}Mg	9.10	28.18	9.20	27.93	3.54	4.66±0.24
^{25}Mg	9.17	27.99	9.32	27.60	3.47	4.37±0.20
^{26}Mg	9.24	27.80	9.36	27.48	3.43	4.78±0.38
^{27}Al	9.24	30.11	9.32	29.89	3.51	4.12±0.21
^{34}S+^{24}Mg	9.21	27.88	9.40	27.38	3.45	3.70±0.16
^{25}Mg	9.28	27.69	9.45	27.26	3.38	3.84±0.20
^{26}Mg	9.35	27.50	9.50	27.11	3.38	3.60±0.28

TABLE II. Parameters used in the zero point motion calculations. The standard deviations σ_2 were calculated according to Eq. (7) of the text. The columns labeled CW and KNS were obtained using radius parameters of the potentials of Christensen and Winther (Ref. 12) and Krappe, Nix, and Sierk (Ref. 13), respectively. T is the period of oscillation for each excited state.

Nucleus	$J_{g.s.}$	J^π	E_x (MeV)	$B(E2,J_{g.s.}\rightarrow J^\pi)$ $(e^2\,\mathrm{fm}^4)$[a]	σ_2 (fm) CW	KNS	T (sec)
^{24}Mg	0^+	2^+	1.37	420±14	0.63	0.60	3.0×10^{-21}
^{25}Mg	$\frac{5}{2}^+$	$\frac{1}{2}^+$	0.59	0.817±0.023			7.0×10^{-21}
		$\frac{3}{2}^+$	0.97	2.28±0.19	0.70[b]	0.67[b]	4.3×10^{-21}
		$\frac{5}{2}^+$	0.61	142±5			2.6×10^{-21}
^{26}Mg	0^+	2^+	1.81	296±13	0.51	0.49	2.3×10^{-21}
^{27}Al	$\frac{5}{2}^+$	$\frac{1}{2}^+$	0.843	12.9±0.6	0.48[b]	0.43[b]	4.9×10^{-21}
		$\frac{3}{2}^+$	1.014	26.0±1.4			4.1×10^{-21}
^{32}S	0^+	2^+	2.23	300±13	0.36	0.35	1.9×10^{-21}
^{34}S	0^+	2^+	2.13	203±13	0.29	0.28	1.9×10^{-21}

[a]From Ref. 16.
[b]Obtained from appropriately weighted individual $B(E2)$ values.

al penetration coefficients $T_l(E,s_1,s_2)$ for partial wave l according to

$$T_l(E)\approx\int_{-\infty}^{\infty}\int_{-\infty}^{\infty}T_l(E,s_1,s_2)W(s_1,s_2)ds_1ds_2\ . \quad (4)$$

In this equation, s_i is the deviation from sphericity of nucleus i and $W(s_1,s_2)$ is an appropriately chosen weight function whose functional form depends on the model used and is described in more detail below. Assuming a specific dependence of the interaction potential on s_1 and s_2 then allows one to calculate the penetration factors $T_l(E,s_1,s_2)$ in the WKB approximation as described by Eq. (2).

Equation (4) implicitly assumes that the shapes of the approaching nuclei are "frozen" during their passage through the interaction barrier, i.e., that the barrier penetration time τ is short compared to the rotational or vibrational periods T of the collective excitation leading to deviations from sphericity for the reactants. This barrier penetration time has been estimated recently[15] by calculating, for simple barriers, the quantum mechanical time delay associated with penetration through classically forbidden regions. Within this approximation, the time τ decreases with decreasing energy and, for the systems investigated here, is less than 4×10^{-22} s for energies more than 3 MeV below the s-wave interaction barrier. This rather surprising result implies that the frozen shape assumption discussed above is well fulfilled for collective modes with excitation energies $\lesssim$6 MeV. Indeed, since the estimate of Ref. 15 is only an upper limit, it is conceivable that even giant resonance modes have to be taken into account in the evaluation of Eq. (4). In any case, fusion at subbarrier energies, where frictional effects presumably are small, is apparently a rapid process, providing additional justification for Eq. (4) (see Table II for the periods T of the excited states considered in the present work).

In the following we will discuss two specific models describing the deviations from sphericity of the reaction partners, namely, static deformations and zero point vibrations. We will first briefly describe the specific form of the interaction potential $V(r,s_1,s_2)$ and weight function $W(s_1,s_2)$ for each model and then compare the predictions with the experimental data.

A. Zero point motion

Following Ref. 8 we assume that the surfaces of the colliding nuclei can be described by independent harmonic vibrations so that the distributions of the nuclear radii is Gaussian. For simplicity the nuclear symmetry axes are constrained along the line connecting the center of mass of the two nuclei, i.e., the interactions are evaluated for colinear spheroids.[8,10] Then the nuclear radii R_i can be written as

$$R_i=R_{0i}\left[1+\alpha_{2i}\frac{\sqrt{5}}{4\pi}\right]=R_{0i}+s_i \quad (5)$$

in terms of the unmodified radii R_{0i} and the quadrupole deformation parameters α_{2i}. Because of the assumption of independent harmonic vibrations, the weighting function $W(s_1,s_2)$ can then be expressed as

$$W(s_1,s_2)=W(s_1)W(s_2) \quad (6a)$$

with

$$W(s)=\frac{1}{(2\pi\sigma^2)^{1/2}}e^{-s^2/2\sigma^2}\ . \quad (6b)$$

Following Esbensen,[8] the standard deviation σ of the zero point motion is related to the reduced electric quadrupole transition matrix element $B(E2)$ according to

$$\sigma=\frac{R_0}{5Z}\left[\frac{5B(E2)}{B_W(E2)}\right]^{1/2}, \quad (7)$$

where Z is the nuclear charge and $B_W(E2)$ the Weisskopf unit, for $E2$ transitions.

In principle, all collective modes with vibrational periods $T > \tau$ should be included in the averaging procedure described in Eq. (4). However, octupole and higher modes are not well known for the nuclei studied in the present work. Furthermore, the corresponding $B(E\lambda)$ values are presumably small so that contributions from these modes, which should be added in quadrature to the standard deviation σ, are neglected in the present investigation.

To determine the penetration factors $T_l(E,s_1,s_2)$ one needs, of course, to specify the interaction between the two deformed spheroids:

$$V_{\text{eff}}(r,s_1,s_2) = V_{\text{nucl}}(r,s_1,s_2) + V_{\text{Coul}}(r,s_1,s_2) + \frac{\hbar^2}{2\mu r^2} l(l+1) . \quad (8)$$

To first order in the deformation variables, the Coulomb part is expanded as[8,14,16]

$$V_{\text{Coul}}(r,s_1,s_2) = \frac{Z_1 Z_2 e^2}{r}\left[1+\frac{3}{5}\frac{s_1 R_{01}+s_2 R_{02}}{r^2}\right] . \quad (9)$$

For the nuclear part we closely followed Esbensen[8] by adopting the potential of Ref. 12 according to

$$V_{\text{nucl}}(r,s_1,s_2) = -V_0 \bar{R}\{1+\exp[(r-R_{01}-s_1-R_{02}-s_2-\Delta R)/a]\}^{-1} \quad (10)$$

with a strength parameter $V_0 = 31.67$ MeV, a diffusivity of $a = 0.63$ fm, and $\Delta R = 0.29$ fm. The reduced radius $\bar{R} = R_{01}R_{02}/(R_{01}+R_{02})$ was evaluated using the prescription

$$R_{0i} = 1.233A_i^{1/2} - 0.98A_i^{-1/3} . \quad (11)$$

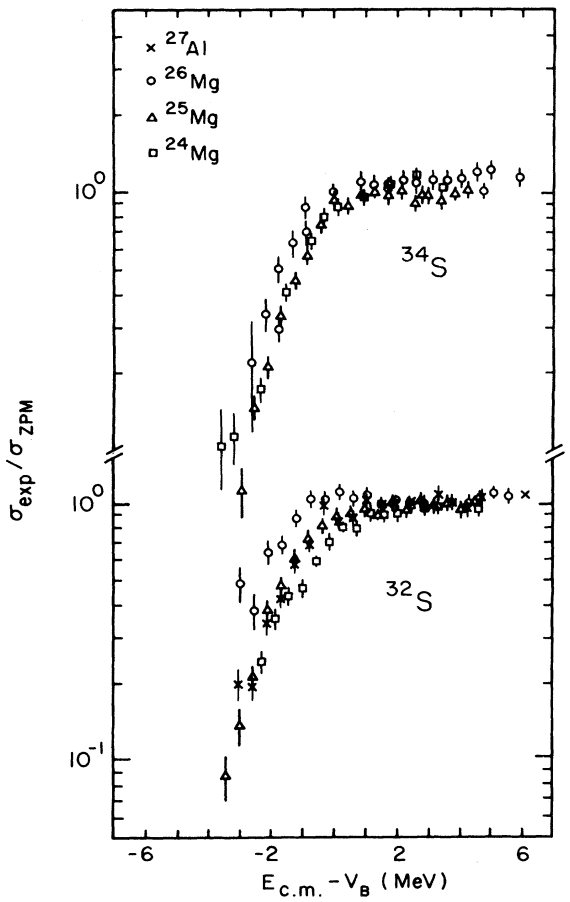

FIG. 10. Total fusion excitation functions normalized to the calculations using the zero point motion model with the Christensen-Winther potential of Ref. 12.

It is important to realize that, within the model described above, no new free parameters are introduced into the calculation of the fusion excitation functions. In addition to the nuclear potential the basic information necessary is the $B(E2)$ values of relevant excited states in target and projectile. They were taken from the work of Ref. 17.

A summary of all of the parameters used in the zero point motion calculations is given in Table II for all systems investigated. The slight rescaling of the s-wave barrier deduced from the one dimensional calculations described in Sec. IV was not incorporated into the calculations including zero point motion (ZPM) since it mainly affects the absolute normalization of the calculated cross sections and not their energy dependence.

The excitation functions for total fusion were calculated by evaluating Eq. (4) using an eight point Gaussian quadrature and substituting the calculated penetration coefficients into Eq. (1).

The results of these calculations are compared in Fig. 10 to the experimental results. The energy axis is again, for each system, shifted by the appropriate s-wave barrier and the experimental data are normalized to the calculated cross section σ_{ZPM} so that for a perfect fit the plotted ratios should be unity for all systems and energies. This is indeed observed for energies $E_{\text{c.m.}} - V_B \gtrsim 0$ but for lower energies the calculated ratios are consistently smaller than one for all systems: taking into account the zero point vibration of projectile and target leads to an overprediction of the measured cross sections. In addition, there are systematic differences in the ratios $\sigma_{\text{exp}}/\sigma_{\text{ZPM}}$ for the various systems at low energies. These differences are substantially bigger than what is obtained when the data are normalized to calculations based on the one-dimensional potentials, as is obvious from Fig. 11. The strong dependence of the cross sections on the $B(E2)$ values of low lying collective states which is predicted in the zero point motion model is not observed in the present data. This conclusion is not related to the fact that, in Fig. 10, the displayed ratios are consistently smaller than one at sub-barrier energies. This can be seen by inspecting Fig. 12, where again all experimental cross sections are normalized to calculations including zero point vibrations. This time, however, the calculations are based on the nuclear potential of Ref.

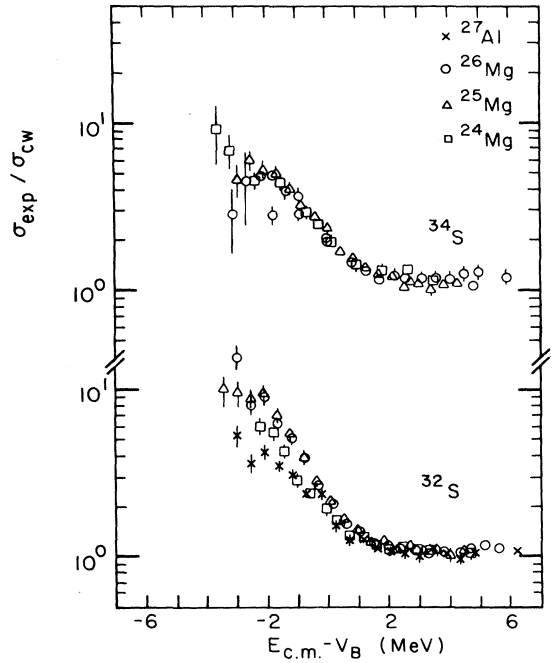

FIG. 11. Total fusion excitation functions normalized to the calculations using a one dimensional model with the Christensen-Winther potential of Ref. 12.

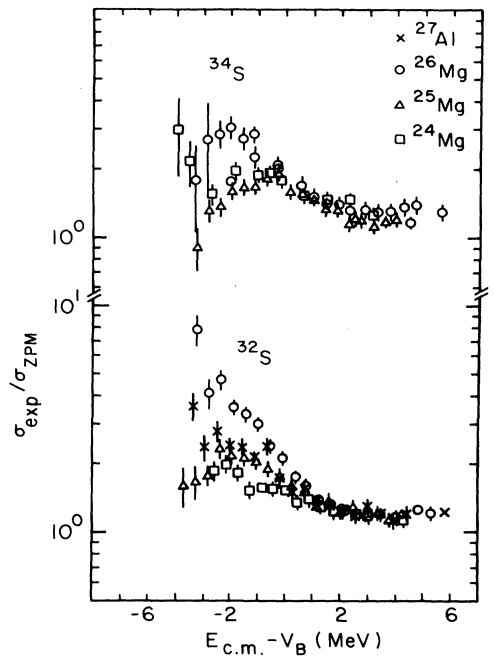

FIG. 12. Total fusion excitation functions normalized to the calculations using the zero point motion model with the Krappe-Nix-Sierk potential of Ref. 13.

13 which has a much thicker barrier. The potential was appropriately modified[18] to take account of the possibility that both target and projectile may independently vibrate about their equilibrium shapes. The result is that the calculations including even the effects of zero point motion still strongly underpredict the experimental data at low energies. In addition, it is obvious from this figure that the differences between the systems are as pronounced as observed in Fig. 10 where the calculations were based on the potential of Ref. 12, indicating that the specific choice of the underlying nuclear potential is not the cause of the discrepancy.

Summarizing, we find that the measured fusion excitation functions cannot be reproduced at sub-barrier energies by including into the calculations of barrier penetrabilities the quantum mechanical zero point vibration of target and projectile. At present, it is not known if this can be traced to effects, neglected in the present calculations, of dynamical deformations of projectile and target[10] or if it is related to the fact that nuclei in the Mg-Si region are not pure vibrators. We would like to point out, however, that the observed discrepancy between data and calculations could only be substantiated by comparing results for systems differing by only a few nucleons. The global effects[5] of sub-barrier enhancement can always be reproduced by a judicious (and probably reasonable) choice of the nuclear potential underlying the zero point motion calculations (see Figs. 10—12).

B. Static deformations

In this section we investigate the effect on the fusion cross section of static deformations of projectile and target. The structure of low lying states in the Mg, Si, and S isotopes has been well investigated[17] and some evidence for rotational structure exists, especially for the case of ^{24}Mg. In order to take permanent deformation of the reactants into account the nuclear radii are again, to lowest order in the deformation parameters, written as

$$R_i(\theta_i,\phi_i)=R_{0i}[1+\alpha_{2i}Y_{20}(\theta_i,\phi_i)] . \quad (12)$$

For each nucleus, the angle θ is measured between the nuclear symmetry axis and the line connecting the center of mass of target and projectile. The deviations from sphericity s_1 and s_2 are, consequently, angle dependent. For simplicity, and following Refs. 3 and 19, we neglect, in the following, the azimuthal dependences and approximate the minimum distance between the two nuclear surfaces by

$$r-R_1(\theta_1)-R_2(\theta_2) .$$

The nuclear potentials are again written as in Eqs. (9) and (10), and the transmission coefficient for partial wave l is expressed as

$$T_l(E)=\int_0^1\int_0^1 T_l(E,s_1(\theta_1),s_2(\theta_2))W(\theta_1,\theta_2)d\cos\theta_1,d\cos\theta_2 , \quad (13)$$

TABLE III. Summary of quadrupole deformation parameters used in the static deformation calculations. They were determined from measured $B(E2)$ values and quadrupole moments (see Table II and Ref. 17) according to the rotational model.

Nucleus	α_2
^{24}Mg	0.40
^{25}Mg	0.37
^{26}Mg	0.34
^{27}Al	0.25
^{32}S	0.24
^{34}S	0.19

where

$$s_i(\theta)=R_{0i}\alpha_{2i}Y_{20}(\theta)\ .$$

Assuming that all orientations are equally probable determines the weight function

$$W(\theta_1,\theta_2)=1\ . \tag{14}$$

The static deformation model is rather similar to the prescription used in the zero point motion calculations, except that the distribution of deviations from sphericity is not a simple Gaussian.

A simple rotational model was invoked to determine the deformation parameters α_{2i} from the corresponding $B(E2)$ values.[17] The deduced deformations are listed in Table III. As in the case of zero point motion calculations the integral in Eq. (13) was evaluated using standard numerical procedures.

The results of these calculations are compared, in Fig. 13, to the measured excitation functions. The nuclear potential underlying these calculations was that of Ref. 12 without any modifications of the s-wave barrier. The overall agreement between data and calculations is clearly better than that obtained by including zero point vibrations of target and projectile (compare Fig. 10). However, for ^{32}S-induced reactions we still observe, at the low energies, that the measured dependence of the fusion cross section on target neutron number is not in agreement with the calculations. Surprisingly, this is not the case for ^{34}S induced reactions where for all systems the calculated ratios are equal to within the accuracy of the data. The origin of this difference is not understood.

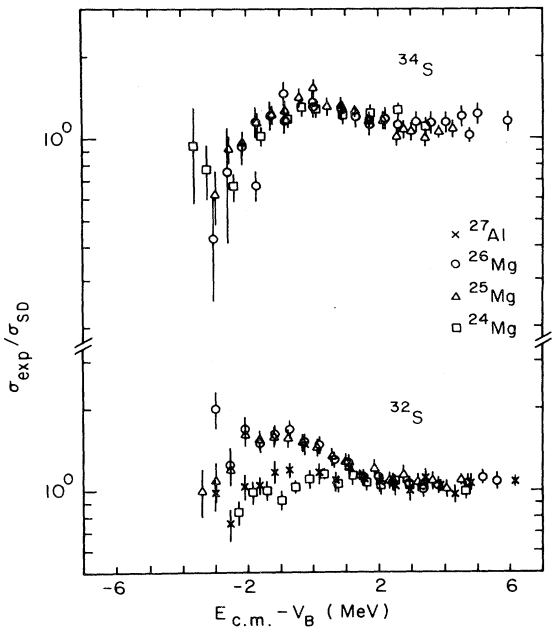

FIG. 13. Total fusion excitation functions normalized to the calculations σ_{SD} for rotating, statically deformed nuclei. The Christensen-Winther potential of Ref. 12 was used.

VI. COUPLED CHANNELS CALCULATIONS

As discussed in the previous section, inclusion of extra degrees of freedom, like zero point motion or static deformations, leads to an explanation of the overall sub-barrier enhancement of the measured fusion cross sections. The dependence of these cross sections on target neutron excess was not reproduced in these models, however, casting some doubt on the influence of the nuclear structure of low lying excited states in target and projectile on the fusion cross sections. One should keep in mind, however, that dynamical effects like the change in deformation of target and projectile during the fusion process have not been taken into account. The role of such dynamical deformations was investigated in Ref. 10 by classical trajectory calculations and found to be rather important; at energies below the s-wave barrier the repulsive Coulomb interaction leads to a dynamic oblate deformation of the fragments, thereby reducing the enhancement observed in the zero point motion or static deformation calculation. In this section we discuss a coupled channels approach, first discussed in Ref. 20, in which all such effects, at least in principle, are taken properly into account, albeit at the expense of introducing a complex optical model potential. We closely follow the prescription of Ref. 19 where an empirical optical potential was chosen to calculate the total reaction cross section σ_R. The cross section for total fusion is then obtained by subtracting from σ_R the cross section for quasielastic excitations. In order to keep the calculations manageable, we neglect all transfer reactions and include into the coupled channels calculations only the excitation of the first excited states in the projectile and target. The main interest in these calculations is to see whether the dependence of the fusion cross section on target neutron excess is predicted correctly. The overall magnitude of the calculated cross sections, of course, depends on the specific choice of the imaginary potential.

The calculations were performed using the coupled channels code CHORK.[21] The parametrization of Ref. 12 was again used to describe the real part of the optical potential. To describe fusion for systems ^{32}S+^{24,26}Mg the imaginary potential was chosen to be of Saxon-Woods shape,

$$W(r)=-W_0[1+\exp(r-R_1-R_2)/a]^{-1} \tag{15}$$

with parameters $W_0=15$ MeV and $a=0.7$ fm. The radii of target and projectile were calculated according to

$$R_i=r_0A_i^{1/3} \tag{16}$$

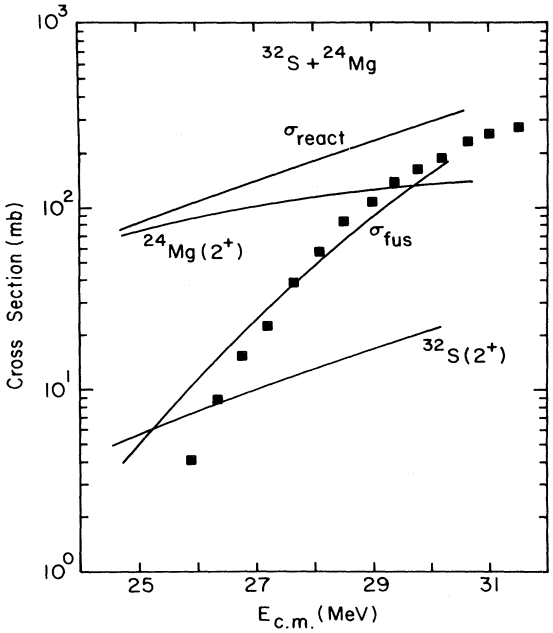

FIG. 14. Comparison of the experimental total fusion cross section with those calculated from the coupled channels model. Shown are the total reaction cross section, inelastic cross section, and the total cross section for the $^{32}S+^{24}Mg$ system. For details see the text.

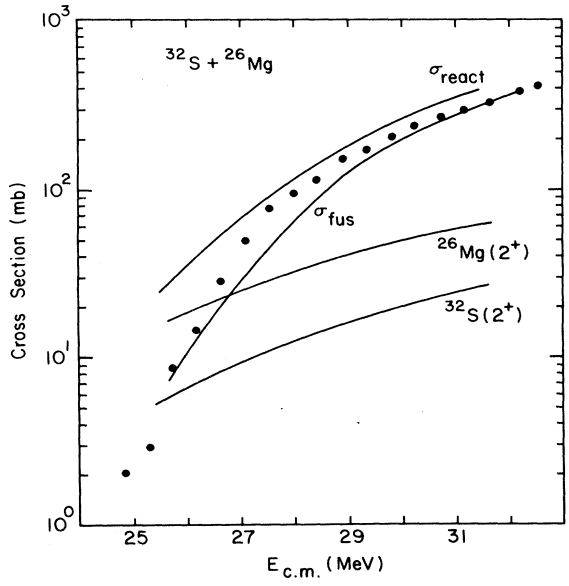

FIG. 15. Comparison of the experimental total fusion cross section with those calculated from the coupled channels model. Shown are the total reaction cross section, inelastic cross section, and the total fusion cross section for the $^{32}S+^{26}Mg$ system. For details see the text.

with $r_0 = 1.0$ fm for both systems. Inelastic excitations including Coulomb excitation were calculated in the framework of a macroscopic collective form factors with deformation parameters as in Table III.

The calculated reaction, inelastic, and fusion cross sections are presented in Figs. 14 and 15 for the systems $^{32}S+^{24,26}Mg$. Inspection of Fig. 14 shows that for the system $^{32}S+^{24}Mg$ a surprisingly good agreement between measured and calculated fusion cross sections is obtained, down to energies well below the s-wave fusion barrier. Note that for $E_{c.m.} < 27$ MeV the total reaction cross section is mostly due to inelastic (Coulomb) excitation of ^{24}Mg to its lowest 2^+ state while excitation of the S nucleus is comparatively small. The situation is quite different for the system $^{32}S+^{26}Mg$ where inelastic cross sections are considerably smaller (see Table III and Fig. 15). In this case, the reaction cross section is considerably smaller and agreement between measured and calculated fusion cross sections is not as good as for $^{32}S+^{24}Mg$, especially in the energy range near the s-wave barrier ($E_{c.m.} \approx 28$ MeV).

For both systems, however, these calculations predict large cross sections at very low energies even though the imaginary potential radius is considerably smaller than the radius of the s-wave barrier (see Table I). This might indicate that the commonly assumed WKB approximation in conjunction with an incoming wave boundary condition is not a reliable means of calculating fusion cross sections and therefore might lead to incorrect conclusions concerning sub-barrier enhancements and the importance of multidimensional barriers.

VII. CONCLUSIONS

In this paper we have presented detailed data for subbarrier fusion between heavy ions in the mass range $24 \leq A \leq 34$. Well below the s-wave barrier the measured cross sections exhibit an enhancement of one to two orders of magnitude over what is predicted by WKB-type calculations using "realistic" one-dimensional nuclear potentials. Within this model, the enhancement can only be reproduced if the barrier is made much thinner than is consistent with other information. Incorporating other degrees of freedom like zero point motion or static nuclear deformations allows one to explain the overall enhancement. Detailed comparison between the measured fusion cross sections and the predictions of calculations including the zero point vibrations of the reactants reveals, however, that in this approach the dependence on target neutron number of the measured fusion cross sections is not well reproduced; better, although not completely satisfactory, an agreement is obtained if one assumes that the nuclei involved are statically deformed. In the context of these models it is also pointed out that reaction times for subbarrier fusion are shorter than commonly assumed because of the shortness of the quantum mechanical barrier transversal time. This in turn indicates that even high lying modes might influence the fusion probability. Finally, fusion cross sections calculated in a quantum mechanical coupled channels approach that includes scattering and excitations in a complex potential agree rather well with the data for $^{32}S+^{24,26}Mg$. In this context, it would be

very useful to measure total reaction cross sections (e.g., via the generalized optical theorem) and inelastic scattering data at sub-barrier energies in order to facilitate a more detailed test of the idea that the cross section for total fusion can be obtained from the difference between reaction and quasielastic cross sections.

This work was supported in part by the National Science Foundation.

---

*Present address: Cyclotron Laboratory, Texas A&M University, College Station, TX 77840.

†Present address: Lawrence Berkeley Laboratory, Berkeley, CA 94720.

‡Present address: Kernfysisch Versneller Inst., Groningen, The Netherlands.

[1]H. J. Krappe, *Lecture Notes in Physics, 117* (Springer, New York, 1980), p. 312.

[2]L. C. Vaz, J. M. Alexander, and G. R. Satchler, Phys. Rep. 69, 373 (1981).

[3]R. G. Stokstad, W. Reisdorf, K. D. Hildenbrand, J. V. Kratz, A. Wirth, R. Lucas, and J. Poitou, Z. Phys. A 295, 269 (1980).

[4]M. Beckerman, M. Salomaa, A. Sperduto, J. D. Molitoris, and A. DiRienzo, Phys. Rev. C 25, 837 (1982); 23, 1581 (1981); Phys. Rev. Lett. 45, 1472 (1980).

[5]U. Jahnke, H. H. Rosner, D. Hilscher, and E. Holub, Phys. Rev. Lett. 48, 17 (1982).

[6]M. Beckerman, M. K. Salomaa, J. Wiggins, and R. Rohe, Phys. Rev. Lett. 50, 471 (1983).

[7]W. Reisdorf, F. P. Hessberger, K. D. Hildenbrand, S. Hofmann, G. Münzenberg, K. H. Schmitt, J. H. R. Schneider, W. F. W. Schneider, K. Summerer, G. Wirth, J. V. Kratz, and K. Schlitt, Phys. Rev. Lett. 49, 1811 (1982).

[8]H. Esbensen, Nucl. Phys. A352, 147 (1981).

[9]R. A. Broglia and A. Winther, in *Heavy Ion Reactions* (Benjamin, London, 1981), Vol. I.

[10]S. Landowne and J. R. Nix, Nucl. Phys. A368, 352 (1981).

[11]A. Gavron, Phys. Rev. C 21, 230 (1980).

[12]P. R. Christensen and A. Winther, Phys. Lett. 65B, 19 (1976).

[13]H. J. Krappe, J. R. Nix, and A. J. Sierk, Phys. Rev. Lett. 42, 215 (1979); Phys. Rev. C 20, 992 (1970).

[14]C. Y. Wong, Phys. Rev. Lett. 31, 766 (1973).

[15]P. Braun-Munzinger and G. M. Berkowitz, Phys. Lett. 125B, 19 (1983).

[16]C. Y. Wong, Phys. Lett. 26B, 120 (1968).

[17]D. Schwalm, E. K. Warburton, and J. W. Olness, Nucl. Phys. A293, 425 (1977).

[18]G. M. Berkowitz, Ph.D. thesis, Stony Brook, 1982 (unpublished).

[19]R. G. Stokstad and E. E. Gross, Phys. Rev. C 23, 281 (1981).

[20]D. Pelte and U. Smilanski, Phys. Rev. C 19, 2196 (1979).

[21]P. D. Kunz, CHORK, coupled channels code, University of Colorado report (unpublished).